colloids and interfaces

MDPI

Article

Preparation of CoMoP/$BiVO_4$ Composite Photoanodes and Investigation of Their Photoelectrochemical Properties

Ke Zhu [1,*], Bingjie Meng [2], Ziying Ren [2], Xing Tian [3] and Yonglei Xing [2,*]

[1] College of Chemistry and Materials, Weinan Normal University, Weinan 714099, China
[2] School of Chemistry and Chemical Engineering, Ningxia University, Yinchuan 750021, China; 12024132102@stu.nxu.edu.cn (B.M.)
[3] Liaocheng Institute for Special Equipment Inspection and Research, Liaocheng 252004, China
* Correspondence: zhuke@wnu.edu.cn (K.Z.); ylxing@nxu.edu.cn (Y.X.); Tel./Fax: +86-0951-2062851 (Y.X.)

Abstract

Herein, a cobalt–molybdenum bimetallic oxide precursor was synthesized via a hydrothermal route, followed by a phosphidation strategy in a tube furnace to produce a CoMoP cocatalyst. Subsequently, a CoMoP/$BiVO_4$ composite photoanode was successfully constructed by loading the CoMoP cocatalyst onto the surface of an electrodeposited $BiVO_4$ film using a drop-casting method. A suite of analytical tools such as TEM, XRD, and XPS was utilized to comprehensively examine the material morphology and crystalline features, verifying that CoMoP was effectively anchored on the $BiVO_4$ surface with intimate interfacial contact. Photoelectrochemical (PEC) performance testing indicated that the composite photoanode achieved optimal performance with a 200 µL loading of the CoMoP dispersion (2 mg/mL). Under front-side illumination, the photocurrent density of the CoMoP/$BiVO_4$ composite photoelectrode reached a photocurrent density of 2.8 mA/cm^2 at 1.23 V (vs. RHE), which is approximately 3.1 times higher than that of unmodified $BiVO_4$ (0.9 mA/cm^2). Under back-side illumination, the composite photoanode generated 3.5 mA/cm^2, representing a 2.3-fold improvement over the 1.5 mA/cm^2 recorded for bare $BiVO_4$. The bandgap energy of $BiVO_4$ was determined to be approximately 2.44 eV based on UV–vis absorption spectra and the corresponding Tauc plot. Owing to its metallic nature, CoMoP exhibits strong broadband absorption in the visible-light region and does not display an intrinsic semiconductor bandgap behavior. Combined with photoluminescence (PL) spectroscopy and PEC results, it was demonstrated that the CoMoP loading effectively promoted interfacial charge separation and transport while accelerating water oxidation kinetics. These results demonstrate that the CoMoP/$BiVO_4$ system serves as an advanced semiconductor material with excellent performance for photoelectrocatalytic water splitting.

Keywords: bismuth vanadate; OER cocatalyst; photoanode; photoelectrochemistry; CoMoP

Check for updates

Academic Editor: Eduardo Guzmán

Received: 26 December 2025
Revised: 30 January 2026
Accepted: 4 February 2026
Published: 6 February 2026

Copyright: © 2026 by the authors. Licensee MDPI, Basel, Switzerland. This article is an open access article distributed under the terms and conditions of the Creative Commons Attribution (CC BY) license.

1. Introduction

The urgent need to develop sustainable energy alternatives is driven by the escalating global energy crisis and the simultaneous deterioration of the environment. Among various renewable energy technologies, photoelectrochemical (PEC) water splitting has attracted considerable attention owing to its potential for clean, efficient, and solar-driven hydrogen production [1,2]. However, the overall efficiency of this process is severely constrained by the sluggish kinetics of the oxygen evolution reaction (OER), which requires a substantial

overpotential and is widely regarded as the bottleneck [3,4]. Consequently, developing efficient and low-cost OER catalysts is critical for advancing PEC technologies.

While noble-metal catalysts (e.g., IrO_2, RuO_2) exhibit exceptional OER activity, their scarcity and high cost preclude widespread application [2,5,6]. This has spurred extensive research into earth-abundant alternatives, particularly transition metal compounds. Among them, transition metal phosphides (TMPs) have emerged as a highly promising class due to their metallic or semi-metallic electronic structures, which endow them with superior electrical conductivity and favorable reaction kinetics compared to their oxide or hydroxide counterparts [7]. Various TMPs, such as Ni_2P, FeP, and MoP, have demonstrated excellent electrocatalytic performance for water splitting [8].

For PEC applications, bismuth vanadate ($BiVO_4$) stands out as a leading photoanode material due to its appropriate bandgap (~2.4 eV) for visible-light absorption, favorable band edge positions for water oxidation, and good chemical stability [9–12]. Nevertheless, the performance of pristine $BiVO_4$ is fundamentally limited by poor charge carrier mobility and slow surface OER kinetics, leading to severe bulk and interfacial recombination [13]. However, pristine $BiVO_4$ suffers from intrinsic limitations such as poor conductivity and slow surface water oxidation kinetics. Theoretical studies indicate that while hole localization in $BiVO_4$ is weak, electron mobility constitutes the primary bottleneck for charge transport in $BiVO_4$. Consequently, the photocurrent density of unmodified $BiVO_4$ photoanodes under AM 1.5 G simulated sunlight is merely 0.81 mA/cm^2, far below the theoretical maximum of 7.5 mA/cm^2. Furthermore, Subramanyam et al. reported a solar-to-hydrogen (STH) conversion efficiency of only 0.82% at 0.61 V vs. RHE for $BiVO_4$ photoanodes, which is significantly lower than the theoretical value of 9.2% [14].

Modification with cocatalysts is a well-established strategy to mitigate these limitations. Effective cocatalysts can extract photogenerated holes, suppress recombination, and accelerate the surface OER, as outlined in the general framework for cocatalyst-enhanced PEC systems [9,15]. In this context, metallic TMPs are ideal candidates due to their dual potential to act as charge-extraction layers and OER catalysts. However, the prevailing discourse in many $BiVO_4$/phosphide studies has predominantly centered on constructing semiconductor–semiconductor heterojunctions (e.g., Type-II), often overemphasizing interfacial band alignment while underappreciating the phosphide's inherent metallic character and its primary role as a charge-transfer mediator and catalyst [1,16]. This conventional heterojunction paradigm may not accurately capture the operating mechanism when the modifier is a metallic compound like CoMoP. Furthermore, the synergistic effects of bimetallic phosphide composition, the volcano-type dependence on cocatalyst loading, and its interplay with illumination direction remain insufficiently explored [17].

Herein, we address these gaps by introducing a bimetallic cobalt–molybdenum phosphide (CoMoP) as a dual-functional metallic modifier for $BiVO_4$ photoanodes. In contrast to previous studies that often focused on single-metal phosphides and overemphasized heterojunction-band-alignment effects, we explicitly demonstrate that CoMoP operates not as a light-absorbing semiconductor, but as a metallic interfacial layer that synergistically combines efficient hole extraction with high OER catalytic activity. Through systematic optimization of composition and loading, together with a detailed analysis of front- versus back-side illumination, we elucidate how this dual function enhances light harvesting, charge separation, and surface reaction kinetics. This work not only provides a rational design strategy for modifying $BiVO_4$ with metallic bimetallic phosphides, but also reframes the mechanistic understanding toward a cocatalyst-centric model, contributing to the development of efficient and stable PEC systems.

2. Experimental Methods

2.1. Preparation of $BiVO_4$

As shown in Figure 1, the $BiVO_4$ electrode was fabricated following a previously published electrodeposition protocol [10]. A BiOI precursor was first grown on FTO conductive glass, followed by a reaction with $VO(acac)_2$ (vanadyl acetylacetonate) under high-temperature conditions to generate $BiVO_4$. The specific procedure was as follows: a total of 20 mmol KI was added to 50 mL deionized water and stirred continuously until fully dissolved. The pH was adjusted to around 1.6 using nitric acid, after which 2 mmol $Bi(NO_3)_3 \cdot 5H_2O$ was introduced to form Solution A. Simultaneously, Solution B was obtained by dissolving 4.6 mmol p-benzoquinone in 20 mL anhydrous ethanol. The electrolyte was produced by slowly adding Solution B into Solution A while maintaining strong agitation. The resulting homogeneous electrolyte was subsequently transferred into a sealed electrochemical cell. The BiOI precursor layer was electrodeposited using a three-electrode system—FTO as the working electrode, Pt as the counter, and Ag/AgCl as the reference—under an applied potential of −0.1 V for 8 min. Then, 200 µL of a $VO(acac)_2$ solution (0.2 mM in DMSO) was uniformly drop-cast onto the BiOI surface. The treated sample was then transferred to a muffle furnace and subjected to annealing at 450 °C for 2 h with a heating rate of 2 °C/min. After naturally cooling to room temperature, the resulting film was soaked in 1 M NaOH to eliminate any remaining V_2O_5 on the surface. Finally, the final pristine $BiVO_4$ photoanode was obtained after thoroughly rinsing the surface with deionized water to remove residues.

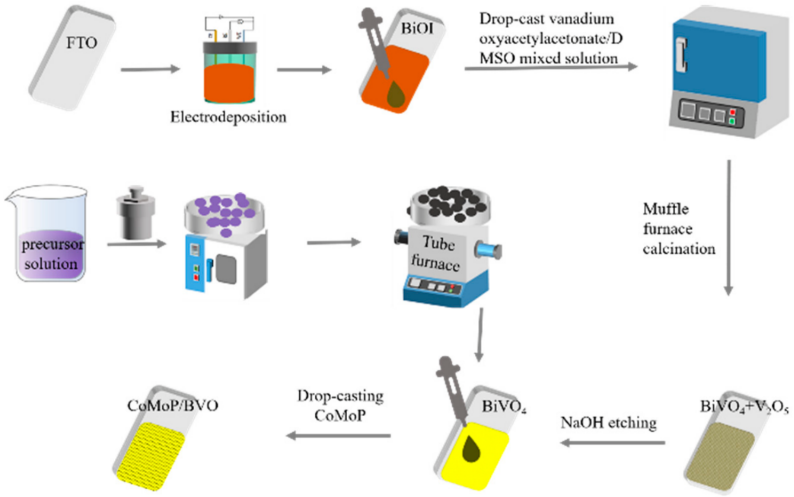


Figure 1. Schematic illustration of the synthesis procedure for pristine $BiVO_4$ and $CoMoP/BiVO_4$ electrodes.

2.2. Preparation of $CoMoP/BiVO_4$

As shown in Figure 1, the synthesis of the bimetallic phosphide CoMoP was carried out using a combination of hydrothermal synthesis and subsequent phosphidation. First, a $CoMoO_4$ precursor was prepared via a hydrothermal method, and the target product CoMoP was obtained by phosphidation in a tube furnace. The detailed procedure involved dissolving $Co(NO_3)_2 \cdot 6H_2O$ and $Na_2MoO_4 \cdot 6H_2O$ in deionized water (20 mL each) at molar ratios of 5:1, 5:3, and 5:5, followed by vigorous stirring to guarantee full dissolution. The resulting solution was transferred to a high-pressure autoclave and reacted at 150 °C for 6 h. After the reaction, the mixture was cooled to room temperature, and the precipitate was washed multiple times alternately with deionized water and absolute ethanol. It was then dried in a vacuum oven and finally ground into a uniform powder. Subsequently, 0.5 g of $NaH_2PO_2 \cdot H_2O$ and the precursor powder obtained from grinding were placed at

the upstream and downstream ends of a tube furnace, respectively. The mixture was then heated under an argon atmosphere to 450 °C at a ramp rate of 5 °C/min and maintained for 2 h to accomplish the phosphidation process. Depending on the initial concentration of $Na_2MoO_4 \cdot 6H_2O$, the final products were designated as CoMoP1, CoMoP2, and CoMoP3 (abbreviated as CMP1–3). The obtained phosphided powder was ultrasonically dispersed in a 1:1 (*v*/*v*) mixture of ethanol and isopropanol to yield a 2 mg/mL catalyst ink; 50 μL of 0.05% Nafion solution was added to the dispersion (per 1 mL total liquid volume). An aliquot of 100 μL of the dispersion was evenly drop-cast onto the of the $BiVO_4$ electrode surface and subsequently dried on a graphite hot plate at 100 °C to form the composite photoelectrode. By regulating the catalyst dispersions with different Co/Mo ratios (CMP1–3) and the number of drop-casting layers, CoMoP/$BiVO_4$ composite photoanodes with varying loadings and compositions were constructed for subsequent performance optimization and characterization.

2.3. Characterization

Detailed information on the characterization and photoelectrical performance is provided in the Supporting Information.

3. Results and Discussion

3.1. Structural and Morphological Analysis

XRD analysis was performed to identify the crystalline phases of the samples, as illustrated in Figure 2. Figure 2a presents the XRD patterns of $BiVO_4$ (BVO), CoMoP powder, and the CoMoP/$BiVO_4$ composite photoelectrode. For the $BiVO_4$ sample, diffraction peaks from SnO_2 belonging to the FTO substrate and all other peaks correspond perfectly to the standard card for monoclinic scheelite $BiVO_4$ (PDF# 14-0688), indicating the successful preparation of high-purity monoclinic $BiVO_4$. Diffraction peaks located at 18.6°, 28.8°, and 37.8° correspond to the (110), (−121), and (220) crystal planes of $BiVO_4$, respectively. In the spectrum of the CoMoP/$BiVO_4$ composite, no distinct impurity peaks were observed. Although the $BiVO_4$ diffraction intensity dominates, weak peaks attributed to CoMoP are visible (marked by ♥ in Figure 2a). The XRD profiles of CoMoP and its precursor are presented in Figure 2b. The XRD profiles of CoMoP and its precursor are presented in Figure 2b. The precursor peaks correspond to the standard card PDF# 14-0086, associated with hydrated cobalt molybdate (e.g., $CoMoO_4 \cdot xH_2O$), confirming the successful hydrothermal synthesis of the bimetallic oxide. The CoMoP product obtained after phosphidation exhibits main peaks consistent with the CoMoP standard card (PDF# 32-0300); for instance, peaks at 39.1° and 41.5° correspond to the (112) and (211) planes, respectively.

The microscopic surface architectures of the synthesized materials were characterized via SEM, as depicted in Figure 2. The hydrothermally synthesized cobalt–molybdenum oxide precursor appears as stacked rectangular block-like structures (Figure 2c). After low-temperature phosphidation, the morphology changes significantly (Figure 2d). CoMoP largely retains the macroscopic outline of the precursor, but the particle size decreases and the surface becomes rough, forming a porous columnar structure aggregated from nanoparticles. This morphological evolution significantly expands the specific surface area, thereby exposing more catalytic active sites. The electrodeposited $BiVO_4$ exhibits a characteristic worm-like nanoporous architecture (Figure 2e), a structure conducive to light harvesting and electrolyte permeation [13]. After loading CoMoP (Figure 2f), the $BiVO_4$ main structure is maintained. Although distinct CoMoP particles are difficult to resolve at this magnification, the composite surface appears rougher compared to pristine $BiVO_4$, suggesting uniform dispersion and attachment of CoMoP on the $BiVO_4$ skeleton. This

composite structure enlarges the electrode-electrolyte interface and provides pathways for interfacial charge transfer, which is expected to improve photoelectrocatalytic performance.

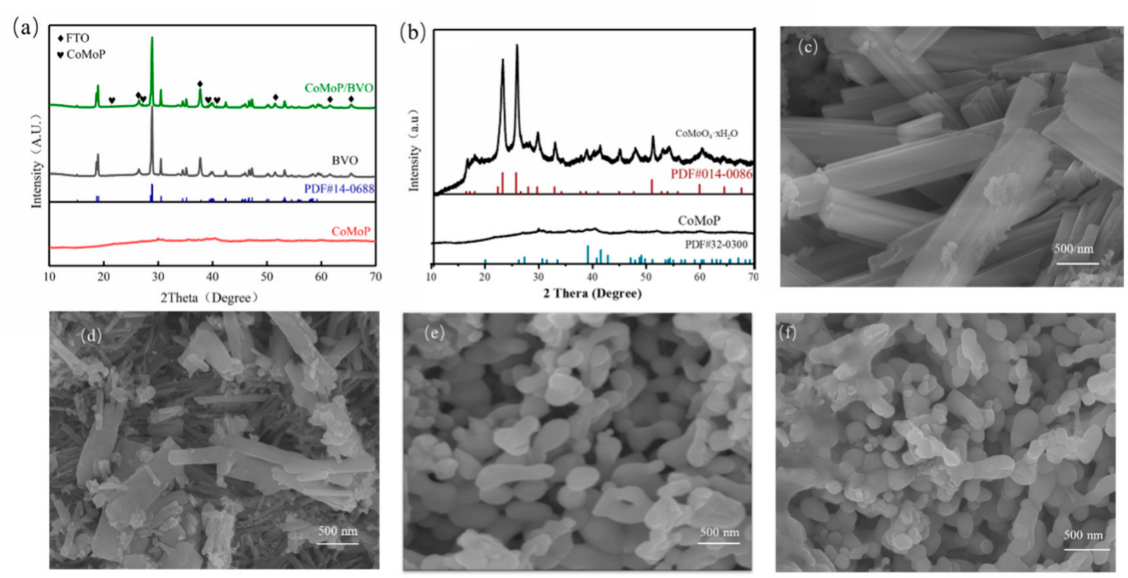


Figure 2. XRD patterns of (**a**) BVO, CoMoP powder, and the CoMoP/$BiVO_4$ composite; (**b**) CoMoP precursor and CoMoP powder. SEM images of (**c**) CoMoP precursor, (**d**) CoMoP, (**e**) $BiVO_4$, and (**f**) the CoMoP/$BiVO_4$ composite.

To further investigate the microstructure and interfacial characteristics, TEM and HRTEM characterizations were performed (Figure 3). Compared to the TEM image of $BiVO_4$ (Figure 3a), the CoMoP/$BiVO_4$ morphology (Figure 3b) shows a rougher surface and slightly blurred edges, indicating successful CoMoP coating. The HRTEM image (Figure 3c) distinctly displays well-resolved lattice fringes at the CoMoP/$BiVO_4$ interface. The measured lattice spacing of 0.23 nm corresponds to the (112) plane of CoMoP, while distances of 0.309 nm and 0.467 nm match the (−121) and (110) planes of monoclinic $BiVO_4$. These observations verify that a tightly coupled heterojunction interface has been successfully constructed. Elemental mapping (Figure 3d) confirms the presence of Co, Mo, P, Bi, O, and V, and shows that Co, P, and Mo are homogeneously dispersed across the $BiVO_4$ framework. This provides sufficient evidence that the CoMoP cocatalyst has been successfully loaded with good interfacial contact.

XPS measurements were performed to probe surface composition and valence states. The survey spectrum (Figure S1) indicates signals from Bi, V, Co, Mo, O, and P, while the prominent F 1s peak arises from the Nafion binder. XPS measurements were performed to probe surface composition and valence states. The survey spectrum (Figure S1) indicates signals from Bi, V, Co, Mo, O, and P, while the prominent F 1s peak arises from the Nafion binder. In Figure 4a, The O 1s region can be deconvoluted into three components at 530.58, 531.88, and 534.18 eV, attributed to lattice oxygen (O_L), surface hydroxyl/adsorbed oxygen (O_H), and oxygen-vacancy-related species or adsorbed water (O_V) [18]. As illustrated in Figure 4b, the Bi 4f signals at 159.18 eV and 164.38 eV suggest the presence of Bi^{3+}. The V 2p spectrum (Figure 4c) displays two characteristic peaks located at 516.58 and 524.08 eV, confirming the V^{5+} state. The Co 2p spectrum (Figure 4d) reveals complex cobalt speciation. The Co $2p_{3/2}$ region features peaks at 778.78 and 780.78 eV, corresponding to Co^0 (metallic or phosphide) and Co^{2+} (likely surface oxidation), respectively, with a satellite peak at 784.48 eV. Binding energies are higher than metallic Co (778.1 eV), indicating Co atoms carry a positive charge [19]. The Mo 3d spectrum (Figure 4e) fits to Mo^{4+} (from CoMoP) and Mo^{6+} (from surface oxidation). In Figure 4f, P 2p peaks are distinguished near 129.7 eV

and 135.08 eV. The 129.7 eV peak (M-P) exhibits a negative binding energy shift compared to elemental phosphorus (130.2 eV) [8] indicating P carries a negative charge ($P^{\delta-}$) bonded to metals; the 135.1 eV peak corresponds to surface phosphates (P-O_x). In summary, Co and Mo tend to be positively charged (δ^+) while P is negatively charged (δ^-), suggesting electron transfer from metal to phosphorus atoms [8,10]. This electronic characteristic is consistent with the metallic electronic structure of CoMoP and thus favors the acceptance and transport of holes.

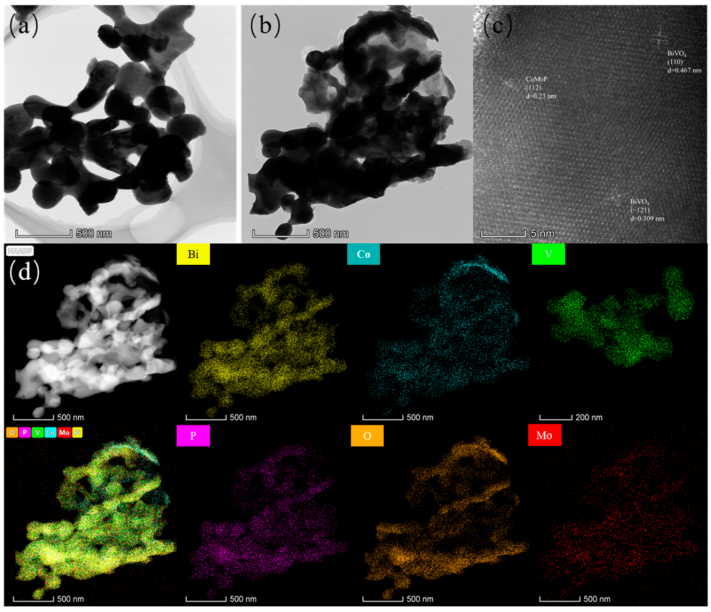


Figure 3. TEM images of (**a**) $BiVO_4$ and (**b**) CoMoP/$BiVO_4$; (**c**) HRTEM image of CoMoP/$BiVO_4$; (**d**) HAADF-STEM image and elemental mappings of Bi, V, Mo, Co, P, and O in CoMoP/$BiVO_4$.

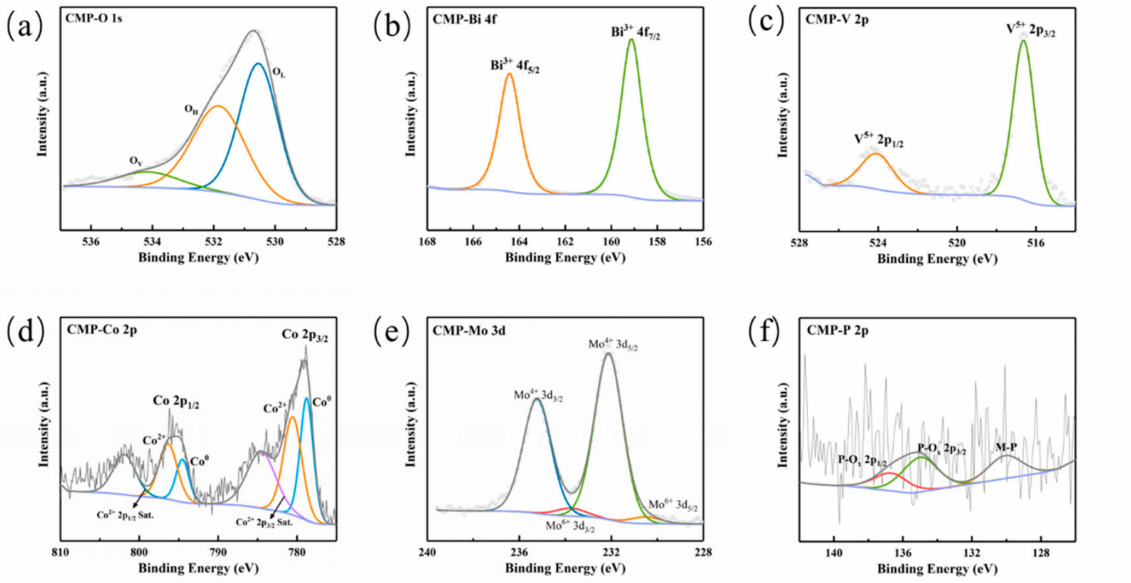


Figure 4. The XPS survey spectra of CoMoP/$BiVO_4$: (**a**) O 1s; (**b**) Bi 4f; (**c**) V 2p; (**d**) Co 2p; (**e**) Mo 3d; (**f**) P 2p.

The optical band gap (E_g) of the catalyst was determined using the standard Tauc plot method derived from UV-visible diffuse reflectance spectroscopy data via the Kubelka-Munk function, $F(R_\infty)$. As shown in Figure 5a–c, By plotting $(F(R\infty)h\nu)2$ against photon energy ($h\nu$), the value of Eg was obtained by extrapolating the linear region of the absorption edge to the abscissa where $(F(R_\infty)h\nu)^2 = 0$. Pure-phase $BiVO_4$ exhibits a distinct

absorption edge at ~500 nm, and the corresponding Tauc plot yields an optical band gap (E_g) of approximately 2.44 eV. Pure CoMoP exhibits strong broadband absorption across the visible range without a distinct absorption edge, consistent with its metallic/semi-metallic characteristics. Therefore, CoMoP acts as a metallic material with broadband absorption rather than a semiconductor with an intrinsic band gap. Importantly, modification of $BiVO_4$ with CoMoP significantly enhances the overall visible-light absorption intensity, which is attributed to the complementary broadband absorption of CoMoP and the improved light-scattering effect at the composite interface [20,21].

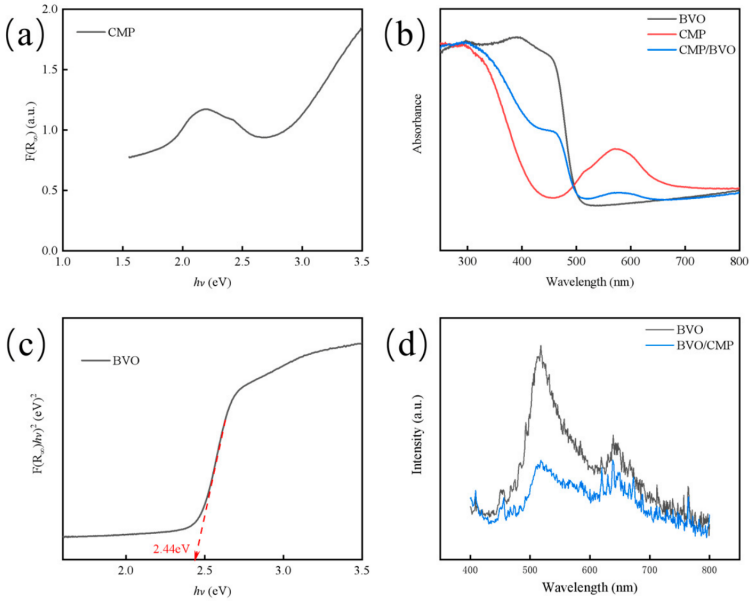


Figure 5. (**a**) Revised K-M function plot of CoMoP; (**b**) UV-Vis DRS of $BiVO_4$, CoMoP and CoMoP/$BiVO_4$ photoanodes; (**c**) Tauc plots of $BiVO_4$; (**d**) PL spectra of $BiVO_4$ and CoMoP/$BiVO_4$ photoanodes.

Photoluminescence (PL) spectroscopy was employed to investigate the charge separation efficiency (Figure 5d). While pure $BiVO_4$ exhibits a high-intensity emission peak attributed to rapid radiative recombination, the CoMoP/$BiVO_4$ composite shows significant fluorescence quenching, indicating a substantial suppression of carrier recombination. This phenomenon is not primarily driven by traditional semiconductor heterojunction interface engineering, but rather stems from the superior hole-extraction capability of CoMoP. Specifically, the metallic CoMoP possesses an optimized work function that creates an ideal energy level alignment with $BiVO_4$, facilitating the rapid extraction of photo-generated holes from the $BiVO_4$ valence band to the CoMoP surface [16].

3.2. Photoelectric Performance

3.2.1. Influence of Different Co/Mo Ratios

To explore the effect of the Co/Mo ratio, CoMoP cocatalysts with molar ratios of 5:1, 5:3, and 5:5 were prepared and loaded (200 μL of 2 mg/mL dispersion) onto $BiVO_4$, labeled BVO/CMP1, BVO/CMP2, and BVO/CMP3. PEC tests were conducted in 0.5 M Na_2SO_4 under visible-light irradiation ($\lambda \geq 420$ nm). LSV results (Figure 6) show that all composites exhibit improved photocurrents over pristine BiVO4. BVO/CMP1 (Co/Mo = 5:1) performed best. Under front illumination (Figure 6a), BVO/CMP1 achieved 2.8 mA/cm^2 at 1.23 V vs. RHE (3.1 times BiVO4′s 0.9 mA/cm^2). Under back illumination (Figure 6b), it reached 3.5 mA/cm^2 (2.3 times BiVO4′s 1.5 mA/cm^2). A distinct cathodic shift in onset potential was also observed, indicating CoMoP lowers the water oxidation overpotential.

Increasing Mo content (ratios 5:1 to 5:5) decreased performance, suggesting 5:1 offers the optimal balance of intrinsic activity and interfacial charge transport.

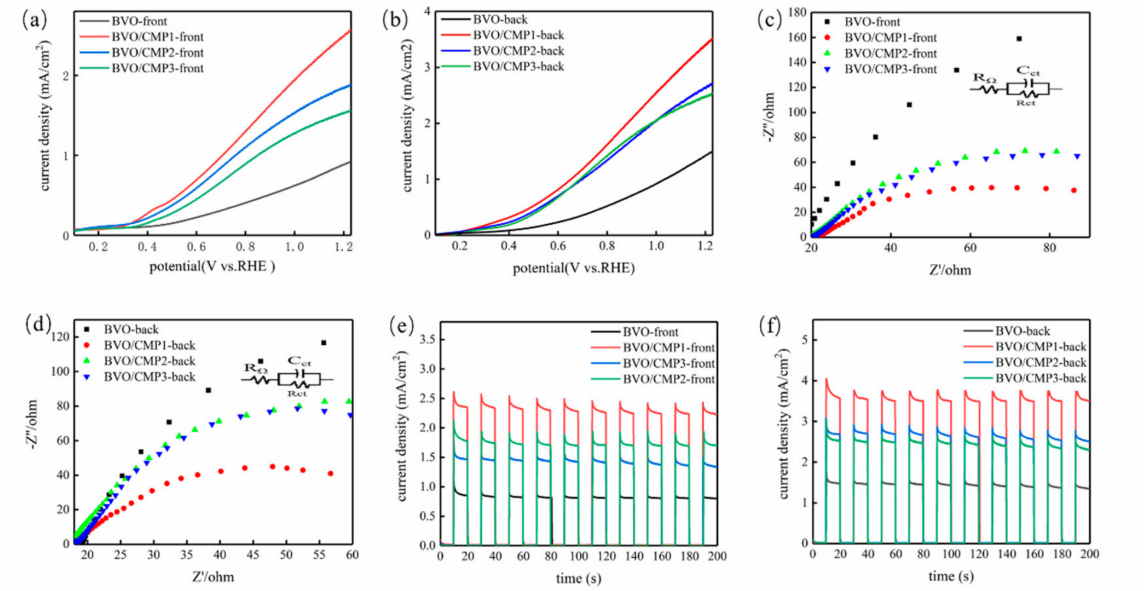


Figure 6. (**a**,**b**) LSV curves, (**c**,**d**) EIS Nyquist plots, and (**e**,**f**) transient photocurrent responses of $BiVO_4$ and CoMoP/$BiVO_4$ under front-side and back-side illumination.

EIS tests (Figure 6c,d) reveal charge transfer kinetics. Smaller semicircles in Nyquist plots indicate lower charge transfer resistance (R_{ct}). All composites showed significantly lower R_{ct} than pristine $BiVO_4$, with BVO/CMP1 exhibiting the lowest resistance, consistent with LSV results. The decreased charge-transfer resistance (Rct) confirms that CoMoP functions as an efficient interfacial charge-transport layer, facilitating the extraction and transfer of photogenerated holes toward the OER electrolyte. Transient photocurrent (i-t) measurements (Figure 6e,f) exhibit rapid and reproducible photoresponses. The pronounced photocurrent spikes observed upon light illumination are indicative of surface hole accumulation and subsequent recombination. Notably, the composite photoelectrode delivers a significantly higher steady-state photocurrent than pristine $BiVO_4$, which can be attributed to the synergistic hole-extraction and catalytic effects of CoMoP. These results collectively demonstrate enhanced hole extraction efficiency and suppressed bulk recombination in the composite system.

3.2.2. Influence of Different CoMoP Loading Amounts

Using the optimal BVO/CMP1 composition, loading was optimized by varying drop-casting layers (1L, 2L, 3L). LSV curves (Figure 7a,b) show a "volcano-type" trend, with BVO/CMP1-2L (200 µL) exhibiting the highest photocurrent. The onset potential stabilized at ~0.3 V vs. RHE (negative shift of ~100 mV vs. $BiVO_4$). Low loading (1L) provides insufficient active sites, while excessive loading (3L) likely causes light shielding (as CoMoP absorbs light, Figure 5a) and increases charge transport path lengths, leading to recombination. EIS results (Figure 7c,d) align with this, showing minimum R_{ct} for the 2L sample. Transient i-t curves (Figure 7e,f) further confirm BVO/CMP1-2L has the highest steady-state current, validating 2 layers as the optimal loading for maximizing the cocatalyst's dual function.

ABPE Results (Figure 8a,b) show that the maximum ABPE values for BVO/CMP1 are 0.25% (front illumination) and 0.28% (back illumination) at ~0.85 V vs. RHE, representing a 3-fold and 3.5-fold enhancement over pristine $BiVO_4$, respectively. The performance difference between illumination directions originates from a trade-off between light harvesting efficiency and charge transport losses. Under front illumination, the optical shading effect

of CoMoP reduces photon absorption by $BiVO_4$ by approximately 30% compared to the pure phase; although the hole transport path is shorter here, insufficient photogenerated carriers result in a photocurrent density of only 2.8 mA/cm^2. In contrast, back illumination bypasses this shielding, allowing $BiVO_4$ to retain 92% of its intrinsic light absorption. Concurrently, this configuration promotes the direct extraction of electrons through the FTO substrate, thereby minimizing transport losses and yielding a superior photocurrent density of 3.5 mA/cm^2. These findings indicate that CoMoP functions primarily as a surface modifier rather than a bulk light-absorbing material, providing a strategic reference for optimizing photoanode orientation (e.g., employing back illumination to mitigate the light shielding of the modification layer) in practical applications. Mott-Schottky plots exhibit positive slopes, confirming the n-type semiconducting nature of both $BiVO_4$ and the CoMoP/$BiVO_4$ composite. The measured flat-band potentials were determined to be 0.267 V vs. RHE for $BiVO_4$ and 0.125 V vs. RHE for CoMoP/$BiVO_4$ (Table S1). The more negative flat-band potential of the composite indicates enhanced downward band bending at the electrode/electrolyte interface, thereby promoting the migration of holes to the surface. This shift aligns with the cathodic shift in the onset potential observed in the LSV curves, further validating the improved charge separation and transport efficiency [22]. Notably, the quasi-linear slope highlighted by the blue line in the composite's Mott–Schottky plot deviates from classical semiconductor behavior. Originating from the metallic/semi-metallic character of CoMoP, this linearity reflects potential-dependent interfacial capacitance rather than pure space-charge capacitance. This capacitive response accelerates hole extraction from $BiVO_4$ and enhances OER kinetics, and thus should not be interpreted as a direct reflection of $BiVO_4$'s intrinsic band structure.Crucially, this energetic modulation is attributed to the incorporation of the metallic CoMoP layer, which acts as an efficient hole-extraction cocatalyst. Long-term stability tests conducted at 1.23 V vs. RHE for 6 h (Figure 8e,f) reveal that pristine $BiVO_4$ suffers significant degradation due to photocorrosion, with a current retention of only ~64%. In contrast, BVO/CMP1 exhibits exceptional stability (retention > 95%) under both illumination directions. This robustness stems from a dual mechanism: firstly, the rapid hole extraction by CoMoP prevents the accumulation of surface holes and the subsequent oxidative corrosion; secondly, the potential formation of a stable Mo-based passivation layer minimizes the impact of illumination-direction-dependent interfacial stress on long-term stability.

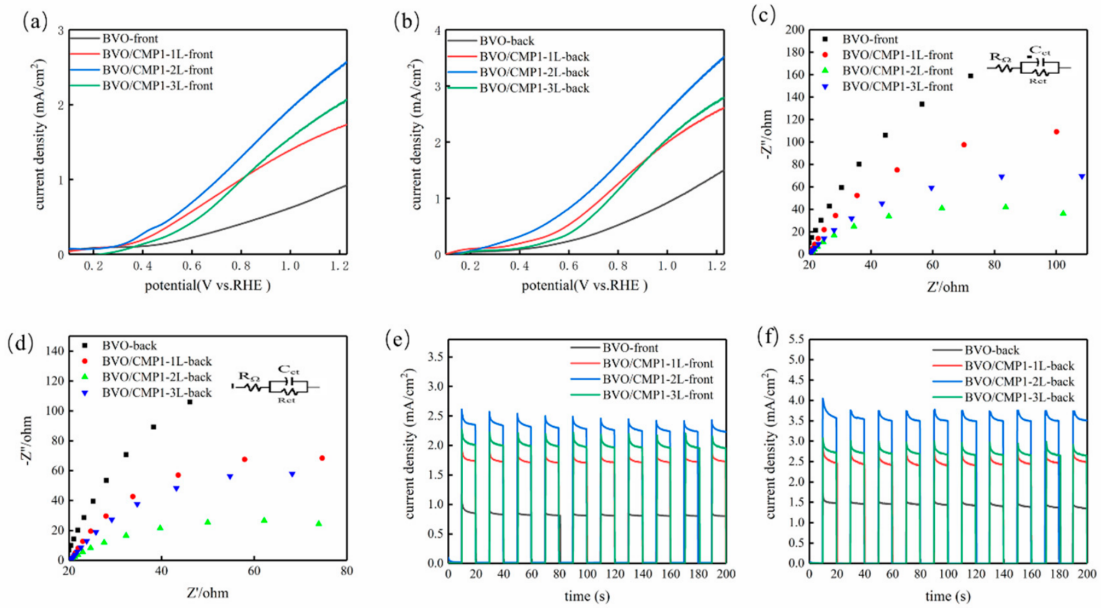


Figure 7. (**a**,**b**) LSV polarization curves, (**c**,**d**) EIS Nyquist plots, and (**e**,**f**) i-t response of composite photoelectrode under front-side and back-side illumination.

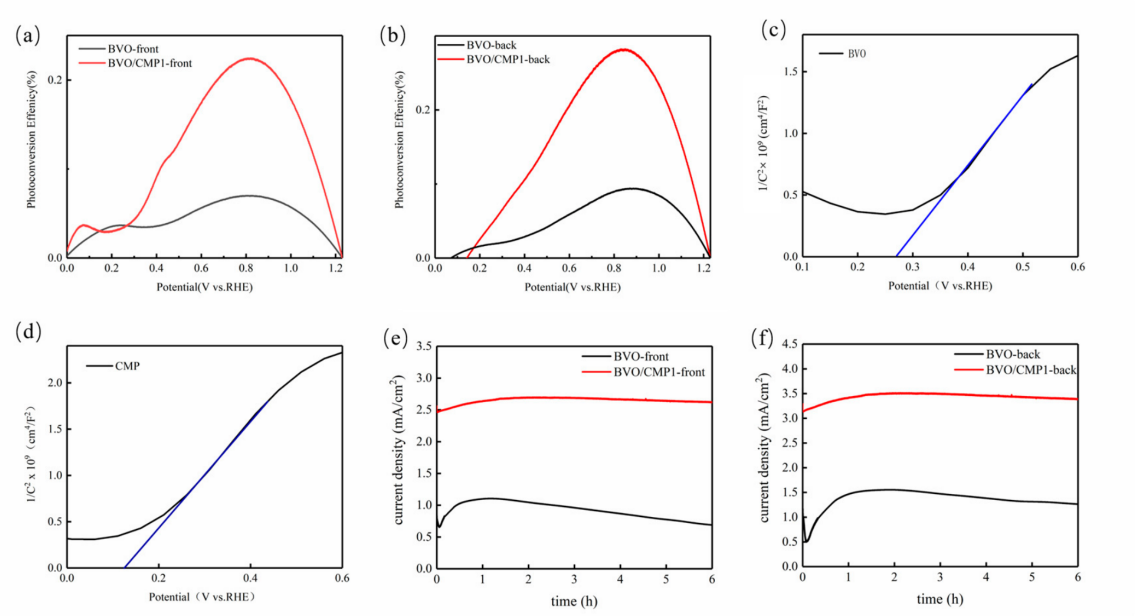


Figure 8. (**a**,**b**) ABPE curves and (**c**,**d**) Mott–Schottky plots of the two pristine materials measured at 1 kHz; (**e**,**f**) photocurrent stability of pristine $BiVO_4$ and BVO/CMP1 under front- and back-side illumination.

In summary, the remarkable enhancement in the PEC performance of the CoMoP/$BiVO_4$ photoanode stems from the synergistic orchestration of CoMoP's dual functionality, serving as both an efficient metallic hole-extraction interlayer and a highly active OER cocatalyst, in Figure 9. This synergy collectively optimizes light-harvesting efficiency, facilitates the separation and transport of photogenerated carriers, and accelerates surface water oxidation kinetics. The proposed mechanism—wherein a metallic cocatalyst extracts holes and subsequently catalyzes surface reactions—is in strict alignment with the canonical theoretical framework for cocatalyst-enhanced PEC systems (e.g., promoting charge transfer, suppressing recombination, and improving long-term stability). Consequently, this provides a coherent and compelling explanation for our experimental observations.

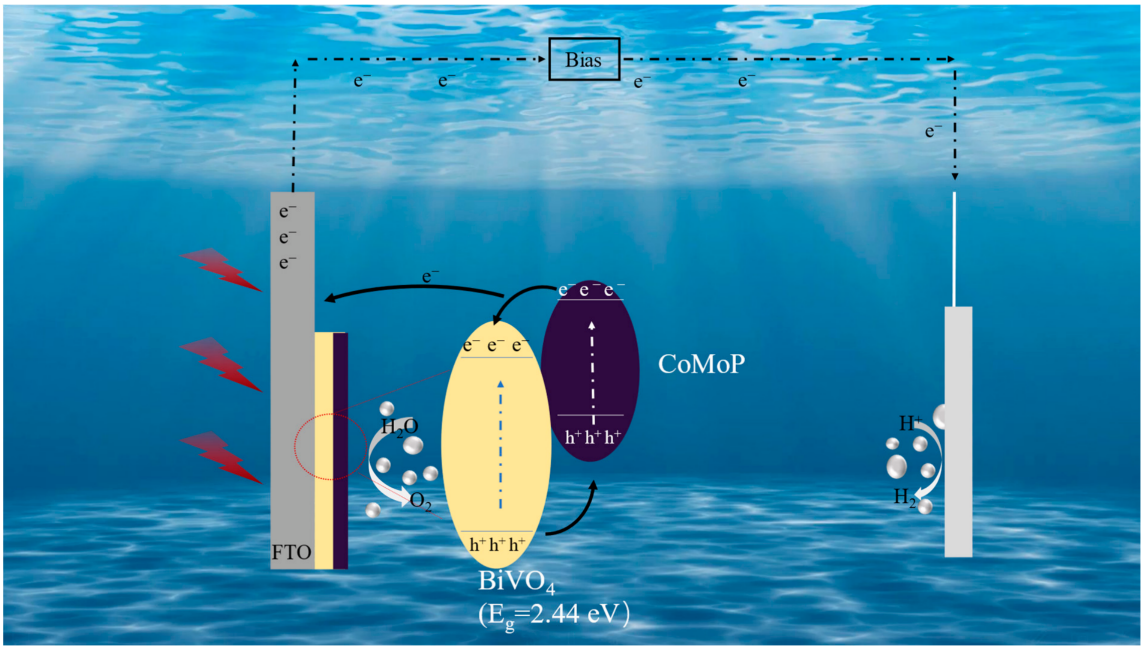


Figure 9. Schematic illustration of the PEC water splitting mechanism over the CoMoP/$BiVO_4$ composite electrode.

4. Conclusions

In this work, nanoporous $BiVO_4$ films were fabricated via electrodeposition, while CoMoP cocatalysts were synthesized through a hydrothermal phosphidation strategy. The CoMoP/$BiVO_4$ composite photoanode was subsequently fabricated via a drop-casting method. Systematic optimization revealed that a Co/Mo ratio of 5:1 with a loading volume of 200 μL delivered the optimal performance. Under 1.23 V vs. RHE, the optimized electrode achieved photocurrent densities of 2.8 mA/cm^2 (front illumination) and 3.5 mA/cm^2 (back illumination), corresponding to 2.3-fold and 3.1-fold enhancements relative to pristine $BiVO_4$, respectively. The composite exhibited an improved Applied Bias Photon-to-Current Efficiency (ABPE) of 0.28% and robust stability with a photocurrent retention of >95% over 6 h. The core finding of this study is that the bimetallic phosphide CoMoP acts as a dual-functional metallic modifier, serving simultaneously as an efficient interfacial hole extraction layer and a highly active oxygen evolution reaction (OER) cocatalyst on the $BiVO_4$ photoanode. This synergistic effect of the dual roles promotes light harvesting, suppresses bulk charge recombination, accelerates interfacial charge transfer, and significantly reduces the OER overpotential. Consequently, a substantial enhancement in photoelectrochemical (PEC) water splitting performance is achieved. This research not only offers a rational design strategy for modifying $BiVO_4$-based photoanodes with metallic transition metal phosphides (TMPs) but also deepens the mechanistic understanding of how bifunctional cocatalysts function via coupled charge extraction and catalytic activation.

Supplementary Materials: The following supporting information can be downloaded at: https://www.mdpi.com/article/10.3390/colloids10010017/s1, Figure S1: The XPS survey spectra full spectrum of CoMoP/$BiVO_4$; Table S1: The flat band potential, CB and VB positions of $BiVO_4$ and CoMoP.

Author Contributions: K.Z.: Methodology, Data curation, Funding acquisition, Writing—Original Draft. B.M. and Z.R.: Methodology, Data curation. X.T.: Resources, Supervision. Y.X.: Resources, Writing—review & editing. All authors have read and agreed to the published version of the manuscript.

Funding: This work was financially supported by the Basic Research Program Project of Weinan City (Grant No. ZWGX2003-1) and the Qin Chuangyuan Research Special Project Program (Grant No. 2024QCY-YJ06).

Data Availability Statement: Data will be made available on request.

Conflicts of Interest: The authors declare that they have no known competing financial interests or personal relationships that could have appeared to influence the work reported in this paper.

References

1. Pan, J.; Li, M.; Wang, Y.; Xie, W.; Zhang, T.; Wang, Q. Advanced photoelectrocatalytic coupling reactions. *Chin. J. Catal.* **2025**, *73*, 99–145. [CrossRef]
2. Ren, S.; Cai, H.; Zhang, H.; Li, H.; Xie, X.; Bian, L.; Tang, C.; Chen, G. Study of Pt:TiO_2/$CuInSe_2$ heterojunction for efficient photoelectrocatalytic hydrogen precipitation. *Int. J. Hydrogen Energy* **2025**, *163*, 150794. [CrossRef]
3. Singh, B.; Nunna, G.P.; Tamta, A.; Chandra, B.; Bahajjaj, A.A.A.; Li, X.; Patri, T.; Arla, S.K.; Joo, S.W. Morphology-dependent photoelectrocatalytic water oxidation for H_2 production: Superior performance of dual-structured zinc vanadate over nickel and copper analogues. *J. Alloys Compd.* **2025**, *1030*, 180816. [CrossRef]
4. Wu, Z.; Ren, K.; Zhou, J.; Zhang, Y.; Qi, L. Orientation Engineering of Nanoporous $BiVO_4$ Photoanodes Toward Boosted Glycerol Valorization and Hydrogen Generation. *Adv. Funct. Mater.* **2024**, *35*, 2418294. [CrossRef]
5. Hilbrands, A.M.; Zhang, S.; Zhou, C.; Melani, G.; Wi, D.H.; Lee, D.; Xi, Z.; Head, A.R.; Liu, M.; Galli, G.; et al. Impact of Varying the Photoanode/Catalyst Interfacial Composition on Solar Water Oxidation: The Case of $BiVO_4$(010)/FeOOH Photoanodes. *J. Am. Chem. Soc.* **2023**, *145*, 23639–23650. [CrossRef]

6. Jung, G.; Moon, C.; Martinho, F.; Jung, Y.; Chu, J.; Park, H.; Hajijafarassar, A.; Nielsen, R.; Schou, J.; Park, J.; et al. Monolithically Integrated $BiVO_4$/Si Tandem Devices Enabling Unbiased Photoelectrochemical Water Splitting. *Adv. Energy Mater.* **2023**, *13*, 2301235. [CrossRef]
7. Nakayama, M.; Yoshida, W. Electrodeposited Manganese Dioxides and Their Composites as Electrocatalysts for Energy Conversion Reactions. *ChemSusChem* **2025**, *18*, e202401907. [CrossRef]
8. Xu, Z.; Li, S.; Lu, W.; Dou, X.; Wu, Y.; Zeng, J.; Dou, Y.; Zhang, J.; Wei, J.; Yu, L. In-Situ construction of hierarchically porous CoNiP/MP Ni electrocatalyst for overall water splitting. *Fuel* **2023**, *348*, 128400. [CrossRef]
9. Xing, Y.; Yi, J.; Zhang, X.; Jin, X.; Peng, Y.; Ni, G.; Yong, X.; Wang, X. Fabrication of $BiVO_4$ photoanode loaded with Zn-doped Co_9S_8 for enhanced photoelectrochemical performance. *J. Photochem. Photobiol. A Chem.* **2024**, *448*, 115322. [CrossRef]
10. Mohamed, N.A.; Arzaee, N.A.; Mohamad Noh, M.F.; Ismail, A.F.; Safaei, J.; Sagu, J.S.; Johan, M.R.; Teridi, M.A.M. Electrodeposition of $BiVO_4$ with needle-like flower architecture for high performance photoelectrochemical splitting of water. *Ceram. Int.* **2021**, *47*, 24227–24239. [CrossRef]
11. Xing, Y.; Ma, H.; Yi, J.; Jin, X.; Peng, Y.; Ni, G. Construction of $BiFeO_3$/$BiVO_4$ composite photoanode and its application in PMS-assisted photoelectrocatalytic degradation of levofloxacin. *J. Environ. Chem. Eng.* **2025**, *13*, 120151. [CrossRef]
12. Xing, Y.; Duan, J.; Wang, D.; Jin, X.; Wang, X.; Yang, R.; Ni, G. Optimizing photoelectrocatalytic Efficiency: Synergistic activation of peroxymonosulfate by $CuFeO_2$/$BiVO_4$ composites for antibiotic removal. *Inorg. Chem. Commun.* **2025**, *171*, 113571. [CrossRef]
13. Li, X.; Wu, J.; Dong, C.; Kou, Y.; Hu, C.; Zang, J.; Zhu, J.; Ma, B.; Li, Y.; Ding, Y. Boosting photoelectrocatalytic oxygen evolution activity of $BiVO_4$ photoanodes via caffeic acid bridged to NiFeOOH. *Appl. Catal. B Environ. Energy* **2024**, *353*, 124096. [CrossRef]
14. Subramanyam, P.; Khan, T.; Neeraja Sinha, G.; Suryakala, D.; Subrahmanyam, C. Plasmonic Bi nanoparticle decorated $BiVO_4$/rGO as an efficient photoanode for photoelectrochemical water splitting. *Int. J. Hydrogen Energy* **2020**, *45*, 7779–7787. [CrossRef]
15. Zhang, Z.; Huang, X.; Zhang, B.; Bi, Y. High-performance and stable $BiVO_4$ photoanodes for solar water splitting via phosphorus–oxygen bonded FeNi catalysts. *Energy Environ. Sci.* **2022**, *15*, 2867–2873. [CrossRef]
16. Kim, H.; Choe, A.; Ha, S.B.; Narejo, G.M.; Koo, S.W.; Han, J.S.; Chung, W.; Kim, J.; Yang, J.; In, S. Quantum Dots, Passivation Layer and Cocatalysts for Enhanced Photoelectrochemical Hydrogen Production. *ChemSusChem* **2023**, *16*, e202201925. [CrossRef]
17. Lee, S.; Lee, Y.; Abbas, H.G.; Ji, S.; Kim, S.Y.; Lee, K.; Li, S.; Lee, E.J.; Choi, J.; Ahn, H.; et al. Photocatalytic Hydrogen Production Using Semiconductor $(CdSe)_{13}$ Clusters. *Nano Lett* **2025**, *25*, 7351–7360. [CrossRef]
18. Ou, G.; Xu, Y.; Wen, B.; Lin, R.; Ge, B.; Tang, Y.; Liang, Y.; Yang, C.; Huang, K.; Zu, D.; et al. Tuning defects in oxides at room temperature by lithium reduction. *Nat. Commun.* **2018**, *9*, 1302. [CrossRef]
19. Chen, J.; Huang, J.; Wang, H.; Feng, W.; Luo, T.; Hu, Y.; Yuan, C.; Cao, L.; Jie, Y.; Kajiyoshi, K.; et al. Phase-mediated cobalt phosphide with unique core-shell architecture serving as efficient and bifunctional electrocatalyst for hydrogen evolution and oxygen reduction reaction. *Chin. Chem. Lett.* **2022**, *33*, 3752–3756. [CrossRef]
20. Feng, C.; Raziq, F.; Huang, H.; Wu, Z.; Alqahtani, H.S.; Alqahtani, R.; Rahman, M.Z.; Chang, B.; Gascon, J.; Zhang, H. Shining Light on Hydrogen: Solar-Powered Catalysis with Transition Metals. *Adv. Mater.* **2025**, *37*, e2410387. [CrossRef]
21. Feng, C.; Luo, J.; Chen, C.; Zuo, S.; Ren, Y.; Wu, Z.-P.; Hu, M.; Ould-Chikh, S.; Ruiz-Martínez, J.; Han, Y.; et al. Cooperative tungsten centers in polymeric carbon nitride for efficient overall photosynthesis of hydrogen peroxide. *Energy Environ. Sci.* **2024**, *17*, 1520–1530. [CrossRef]
22. Liang, Z.; Li, M.; Ye, K.H.; Tang, T.; Lin, Z.; Zheng, Y.; Huang, Y.; Ji, H.; Zhang, S. Systematic engineering of $BiVO_4$ photoanode for efficient photoelectrochemical water oxidation. *Carbon Energy* **2023**, *6*, e413. [CrossRef]

Disclaimer/Publisher's Note: The statements, opinions and data contained in all publications are solely those of the individual author(s) and contributor(s) and not of MDPI and/or the editor(s). MDPI and/or the editor(s) disclaim responsibility for any injury to people or property resulting from any ideas, methods, instructions or products referred to in the content.